Nanotechnology

PURPOSE-LED
PUBLISHING™

PAPER

Tunable phase-change metasurfaces coupled with mid-infrared molecular vibrations

To cite this article: Haotian Tang *et al* 2025 *Nanotechnology* **36** 505203

IOP Publishing Nanotechnology

Nanotechnology **36** (2025) 505203 (8pp) https://doi.org/10.1088/1361-6528/ae2514

Tunable phase-change metasurfaces coupled with mid-infrared molecular vibrations

Haotian Tang[1], **Liliana Stan**[2], **David A Czaplewski**[2], **Xiaodong Yang**[1,*] **and Jie Gao**[3,*]

[1] Department of Mechanical and Aerospace Engineering, Missouri University of Science and Technology, Rolla, MO 65409, United States of America
[2] Center for Nanoscale Materials, Argonne National Laboratory, Argonne, IL 60439, United States of America
[3] Department of Mechanical Engineering, Stony Brook University, Stony Brook, NY 11794, United States of America

E-mail: yangxia@mst.edu and jie.gao.5@stonybrook.edu

Received 12 September 2025, revised 10 November 2025
Accepted for publication 27 November 2025
Published 9 December 2025

Abstract

Chiral optical metasurfaces have emerged as a promising platform in coupling with molecular vibrational fingerprints through the enhanced light-matter interaction under different circularly polarized light illumination. This work reports the mode coupling between the mid-infrared phonon vibrations of polymethyl methacrylate (PMMA) molecules and the thermally tunable chiral metasurfaces based on the phase-change material $Ge_2Sb_2Te_5$ (GST-225). Phase-change chiral metasurfaces with high circular dichroism (CD) in absorption and tunable plasmonic resonance in the frequency range of 48–56 THz are demonstrated, which covers the phonon vibrational frequency of PMMA molecules at 52 THz. The mode splitting features are observed in the absorption and CD spectra when the metasurface resonance is tuned across the phonon vibrational frequency of PMMA molecules during the phase transition of GST-225. The underlying mechanism of molecule-metasurface coupling is further revealed by studying the electric field and power loss density distributions of the phonon–plasmon coupled modes under both left-handed and right-handed circularly polarized (LCP and RCP) light. The demonstrated results show the potential of dynamically tunable chiral metasurfaces for the applications in label-free molecular sensing, biomedical diagnostics, thermal imaging, and mid-infrared photonics.

Keywords: chiral metasurface, phase-change metasurface, molecule-metasurface coupling

1. Introduction

Optical metasurfaces are artificially engineered materials with specific electromagnetic properties that can manipulate light-matter interactions at subwavelength scales [1, 2]. Through careful material selection and precise geometric design of unit cells, optical metasurfaces enable unprecedented control over electromagnetic wave properties, including negative refraction [3, 4], phase manipulation [5–8], perfect absorption [9–12], and polarization conversion [13–15]. Chiral metasurfaces are designed with symmetry-breaking nanostructures to exhibit strong chiroptical responses under LCP and RCP light beyond natural materials [16, 17]. Therefore, optical chiral metasurfaces have emerged as a promising platform for a range of applications including drug development, enantiomeric discrimination, and molecular detection [18–21]. In

---

[*] Authors to whom any correspondence should be addressed.

recent years, $Ge_2Sb_2Te_5$ (GST-225) has been recognized as an optical phase change material that exhibits exceptional contrast in permittivity between amorphous and crystalline states [22, 23]. The integration of GST into chiral metasurfaces represents a promising strategy for realizing dynamic tunability of metasurface resonance, thereby expanding the operational frequency range and enabling various reconfigurable functionalities such as active control of circular dichroism and polarization modulation. On the other hand, optical metasurfaces have also been utilized for the mid-infrared molecular sensing by enhancing the coupling between plasmonic resonances and phonon vibrations of target molecules through near-field interaction [24–26]. The highly confined electromagnetic field near the metasurface nanostructures will greatly enhance the light-matter interaction with molecular vibrational modes, which leads to pronounced spectroscopic features for revealing molecular fingerprints with high sensitivity.

In this work, the coupling between the mid-infrared phonon vibrational mode of PMMA molecules and the tunable plasmonic resonance of phase-change chiral metasurface is investigated. By utilizing the phase-change material GST-225, the designed chiral metasurface exhibits tunable plasmonic resonance across the frequency range from 48 to 56 THz, which is coupled to the phonon vibrational mode of PMMA molecules at 52 THz. The mode splitting features in the absorption and CD spectra under LCP and RCP light are studied when the metasurface resonance is tuned across the phonon vibrational frequency during the phase transition of GST-225 as a function of baking time. The electric field and power loss density distributions of the phonon–plasmon coupled modes under LCP and RCP light are further analyzed to understand the underlying mechanism of molecule-metasurface coupling. The demonstrated results will provide new opportunities for utilizing dynamically tunable chiral metasurfaces in many applications such as label-free ultrasensitive molecular sensing [27, 28], biomedical diagnostics [29–31], thermal imaging and emission control [32–35].

2. Results and discussion

The schematic of the designed chiral metasurface consisting of four thin film layers is presented in figure 1. (a), including a 40 nm top aluminum (Al) layer with chiral cross slot resonators, a 20 nm alumina (Al_2O_3) capping layer, a 230 nm GST-225 dielectric spacer layer, and a 200 nm bottom Al layer deposited on a silicon substrate. The Al layers are deposited using electron beam evaporation. The Al_2O_3 layer is grown by RF sputtering of an Al_2O_3 target. The GST-225 layer is deposited by RF sputtering of a GST-225 target using Ar. The thin Al_2O_3 capping layer is employed to prevent the GST layer from oxidation during the phase transition process [36]. The GST-225 layer is used as the thermally induced phase transition material to achieve the tunability of metasurface resonance in mid-infrared frequency region. The thick bottom Al layer eliminates the transmitted light so that the absorption of the metasurface is obtained by A (absorption) = 1−R (reflectance). The top Al layer is patterned with the designed chiral cross slot resonators to obtain chiroptical responses of the metasurface. The metal-dielectric-metal Fabry–Pérot structure is formed to achieve enhanced absorption at the metasurface resonance through multiple reflections with constructive interference [37]. The chiral structure design starts with a symmetric cross slot structure consisting of one long horizontal slot and one short vertical slot, which is marked as the dotted black lines in figure 1(b). The short vertical slots are tilted with angle α to form two staggered slots connected to the long horizontal slot, which are labeled with the dashed red lines. In the metasurface unit cell, the width of the long horizontal slot is $a = 0.36$ μm, the width of the two staggered slots is $b = 0.24$ μm and their tilted angle is $\alpha = 27°$, while the horizontal and vertical periods are $Px = 2.6$ μm and $Py = 1$ μm. The designed chiral metasurfaces are fabricated using focused ion beam milling (FEI Helios Nanolab 600) into the top Al and Al_2O_3 layers with the condition of 30 kV and 97 pA. The top view of the scanning electron microscope (SEM) image of the fabricated chiral metasurface is presented in figure 1(c).

To investigate the coupling between the mid-infrared phonon vibrational mode of PMMA molecules and the plasmon resonance of the chiral metasurface, an 80 nm thick PMMA layer is spin coated on the top of the chiral metasurface. The absorption spectra of the fabricated chiral metasurface with GST-225 in the amorphous state before and after the PMMA coating under LCP and RCP incident light are characterized by a Fourier transform infrared spectrometer (FTIR, Nicolet 6700) connected to an infrared microscope, as shown in figure 1(d). The LCP and RCP light are obtained using the combination of a linear polarizer and a quarter-wave plate. It is shown that the bare metasurface exhibits the plasmonic resonance at the frequency around 57.8 THz with a high absorption under LCP illumination but a weak absorption under RCP illumination, yielding a large CD in absorption of 0.48. After coating with the PMMA layer, the plasmon resonance of the metasurface slightly redshifts from 57.8 THz to 55.6 THz due to the increased refractive index above the metasurface, while the high CD in absorption is maintained with a value of 0.54. Notably, a distinguished absorption peak emerges around the frequency of 52 THz under both LCP and RCP illumination, which corresponds to the C=O bond phonon vibrational resonance in PMMA molecules [38]. The observed spectral feature indicates the metasurface-enhanced light-matter interaction between the plasmonic resonance and the molecular vibrational mode. In addition, the absorption spectra from the chiral metasurface before and after the PMMA coating under both LCP and RCP illumination are simulated using CST Studio Suite, which are depicted in figure 1(e). In the numerical simulation, the permittivity values of Al, GST-225, Al_2O_3 and PMMA are taken from [39–42]. The imaginary part of the Al permittivity is increased by two times and the real part of the GST-225 permittivity is adjusted in order to match the simulated results with the experimental data.

To further study the enhanced light-matter interaction between the chiral metasurface and the PMMA molecules,

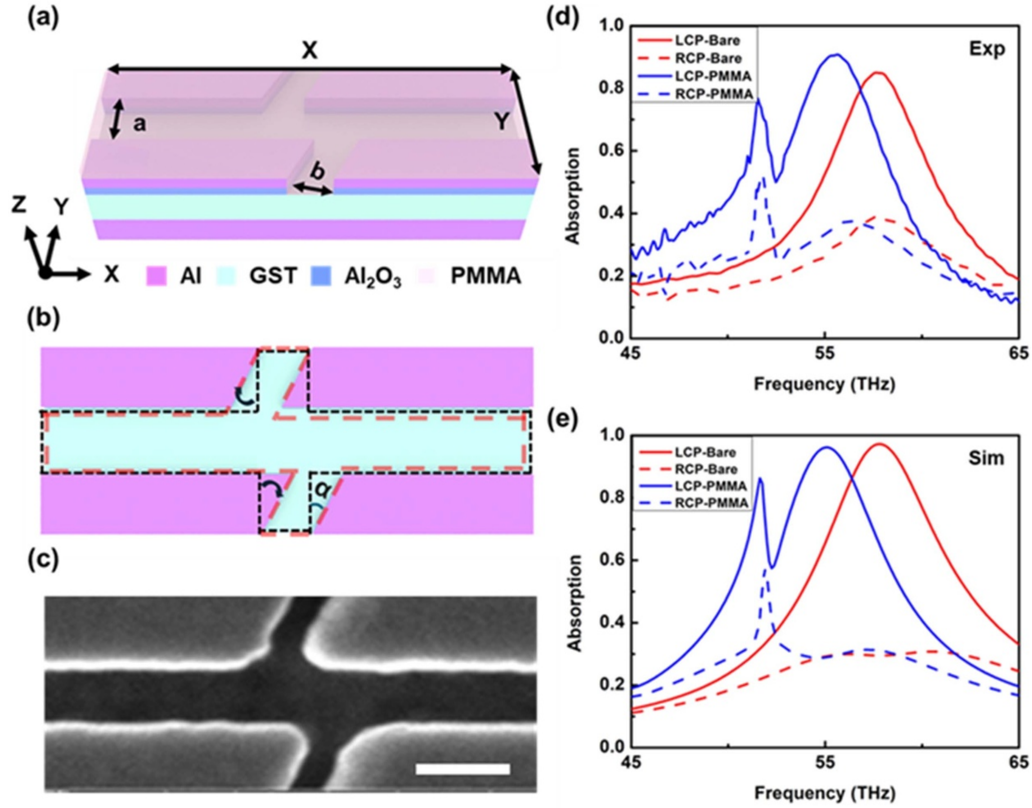

Figure 1. (a) Schematic illustration of the designed chiral metasurface coated with PMMA molecules. (b) Top-view schematic of the chiral cross slot structure. (c) SEM image of the fabricated chiral metasurface. Scale bar is 500 nm. (d) Measured and (e) simulated absorption spectra of the chiral metasurface before and after the PMMA coating under LCP and RCP incident light.

the plasmonic resonance of the metasurface is tuned across the PMMA phonon vibrational resonance by controlling the phase transition in the GST-225 layer from the amorphous state to the crystalline state with the increased baking time of the sample at the temperature of 408 K. Figures 2(a) and (b) display the measured and simulated absorption spectra of the chiral metasurface coated with the PMMA layer under LCP and RCP incident light at various baking times from 0 to 14 min. It is shown that the plasmonic resonance of the chiral metasurface is continuously redshifted from 56 to 48 THz as the baking time increases, which is due to the gradually increased permittivity of the GST-225 layer resulting from the thermally induced phase transition from the amorphous state to the crystalline state. Distinct spectral features are observed as the plasmonic resonance of the metasurface is tuned across the PMMA phonon vibrational frequency at 52 THz, which demonstrates the thermally controlled molecule-metasurface coupling under both LCP and RCP illumination. At the baking time of 4 min, the plasmonic resonance of the metasurface redshifts to 55 THz, and a Fano-like spectral feature around the PMMA phonon vibrational frequency is observed under LCP illumination. As the baking time reaches 7–8 min, the plasmonic resonance of the metasurface is tuned to around 52 THz, overlapping with the PMMA phonon vibration frequency, where distinguished mode splitting features are achieved under LCP illumination. The strong light-matter interaction between the plasmonic resonance of the metasurface and the PMMA phonon vibrational mode in the near field leads to the electromagnetically induced transparency (EIT)-like spectral feature, where the absorption dip around the PMMA phonon vibrational frequency of $\omega_0 = 52$ THz is observed between two absorption peaks corresponding to the coupled phonon–plasmon modes at the resonance frequencies of $\omega^+ = 53.1$ THz and $\omega^- = 51.3$ THz. The mode splitting feature and the anti-crossing behavior are clearly observed due to the coupling between the plasmonic resonance and the phonon vibrational mode. In contrast, under RCP illumination, the coupling between the weak metasurface resonant mode and the PMMA phonon vibrational mode results in the electromagnetically induced absorption (EIA)-like spectral feature where an absorption peak at $\omega_0 = 52$ THz is observed. This circular polarization-dependent spectral features confirm that the plasmonic resonant mode excited by LCP light couples more effectively with the molecular vibrations than RCP light. With the baking time of 10–14 min, the metasurface resonance peak continues to redshift away from the molecular vibrational frequency, which leads to the Fano-like spectral feature in the absorption spectra due to the off-resonance coupling. The observed spectral features during the metasurface phase transition controlled by the baking time demonstrate the dynamically tuned molecule-metasurface interactions.

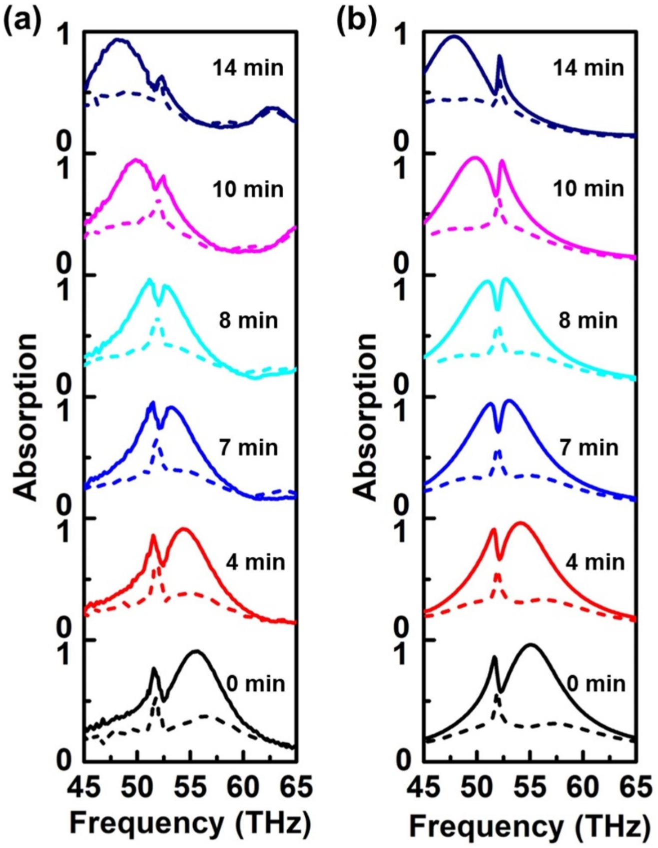

Figure 2. (a) Measured and (b) simulated absorption spectra of the chiral metasurface coated with the PMMA layer under LCP illumination (solid line) and RCP illumination (dashed line) at different baking time.

To understand the underlying mechanism of the coupling between the plasmonic resonance of the metasurface and the PMMA phonon vibrational mode, the simulated electric field and power loss density distributions in both *XY* and *XZ* planes for the chiral metasurface coated with the PMMA layer with GST-225 in the amorphous state are presented in figure 3. For the metasurface resonance mode around 55.1 THz, the electric field shown in figure 3(a) is concentrated around the sharp corners of the chiral cross slot structure, along the sides of the horizontal slot, and inside the Al$_2$O$_3$ capping layer under LCP illumination which leads to strong absorption, while the much weaker electric field distribution is observed under RCP illumination. As shown in figure 3(c), the power loss density of the metasurface resonance mode is mostly located in the Al layer near the Al–Al$_2$O$_3$ interface under LCP incidence but does not exist in the slot areas filled with PMMA molecules, indicating that the strong absorption originates from the plasmonic resonance of the chiral metasurface. As the metasurface plasmonic resonance at 55.1 THz is away from the PMMA phonon vibrational mode at 52 THz, the off-resonance plasmon-phonon coupling results in a Fano-like resonance. Figure 3(b) shows the electric field distribution of the Fano-like resonant mode at the absorption peak of 51.6 THz. The power loss density shown in figure 3(d) is not only located in the Al layer near the Al–Al$_2$O$_3$ interface but also concentrated along the sides and around the corners of the horizontal and staggered slots filled with PMMA molecules under LCP illumination, showing that the absorption is attributed to both PMMA phonon vibrational mode and metasurface plasmonic mode.

To further understand the mode-splitting spectral features of phonon–plasmon coupling, the electric field and power loss density distributions at the Al–Al$_2$O$_3$ interface of the metasurface are simulated when on-resonance coupling occurs between the PMMA phonon vibrational mode and the plasmonic resonance mode at the baking time of 7 min. As shown in figures 4(a) and (b), at the two coupled phonon-plasmon mode resonance frequencies $\omega^+ = 53.1$ THz and $\omega^- = 51.3$ THz, the electric field and power loss density distributions display similar features. Strong electric field is observed near the sharp corners of the chiral cross slot structure under LCP illumination, while relatively weaker electric field is primarily confined along the sides of horizontal slot under RCP illumination. The power loss density distribution at the two frequencies ω^+ and ω^- is mainly concentrated in the Al layer near the Al–Al$_2$O$_3$ interface as well as the sharp corners inside the chiral cross slot structure under LCP incidence, leading to the strong absorption obtained at the two coupled phonon–plasmon modes. In contrast, the power loss density for the RCP case exhibits much weaker confinement with lower intensity. As shown in figure 4(c), distinct field distributions are observed at the phonon vibrational frequency of $\omega_0 = 52$ THz, compared to the cases for ω^+ and ω^-. The electric field intensity and the power loss density in the Al layer near the Al–Al$_2$O$_3$ interface are much weaker, while the power loss density is mainly localized within the slot areas, particularly near the sharp corners and along the sides of the horizontal slot where PMMA molecules are filled. The enhanced coupling between the metasurface plasmonic resonance and the molecular phonon vibrations leads to the destructive EIT-like spectral dip with a lower absorption compared to the absorption at ω^+ and ω^- under LCP illumination, but results in the constructive EIA-like spectral peak with an increased absorption under RCP illumination. The electric field and power loss density analysis reveals the mechanism of the observed mode-splitting spectral features arising from the enhanced near-field coupling between the plasmonic resonant mode and the molecular phonon vibrational mode.

To show the dynamic tuning and anti-crossing behavior of phonon–plasmon coupling during the GST-225 phase transition process, contour plots of the measured absorption spectra and CD spectra as a function of baking time under both LCP and RCP illumination are presented in figure 5(a). Under LCP illumination, when the plasmonic mode is off resonance from the phonon vibrational mode, the plasmon–phonon interaction results in a Fano-like resonance. As the plasmonic mode is on resonance with the phonon vibrational mode at the baking time of 7–8 min, EIT-like resonance is displayed with the two phonon–plasmon modes at the frequencies ω^+ and ω^-. The anti-crossing behavior of two phonon–plasmon mode branches is presented with a mode splitting gap of $\omega^+ - \omega^- = 1.8$ THz, resulting from the coupling between the plasmonic mode and the phonon vibrational mode. In contrast, under the RCP illumination, a consistent EIA-like resonance

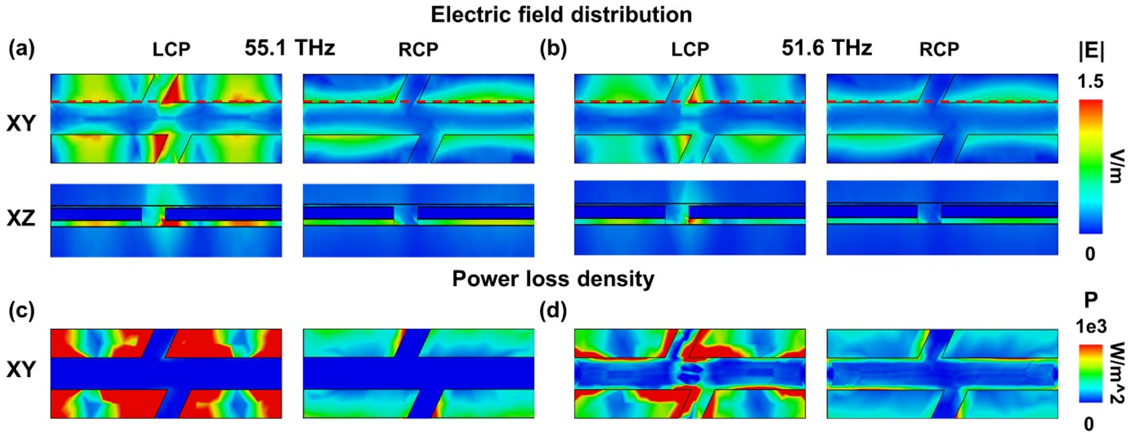

Figure 3. Simulated electric field distributions under LCP and RCP illumination in *XY* plane at the Al–Al2O3 interface and the cross-section in *XZ* plane along the red dashed line at the frequency of (a) 55.1 THz and (b) 51.6 THz. Simulated power loss density distributions under LCP and RCP illumination in *XY* plane at the Al–Al2O3 interface at (c) 55.1 THz and (d) 51.6 THz.

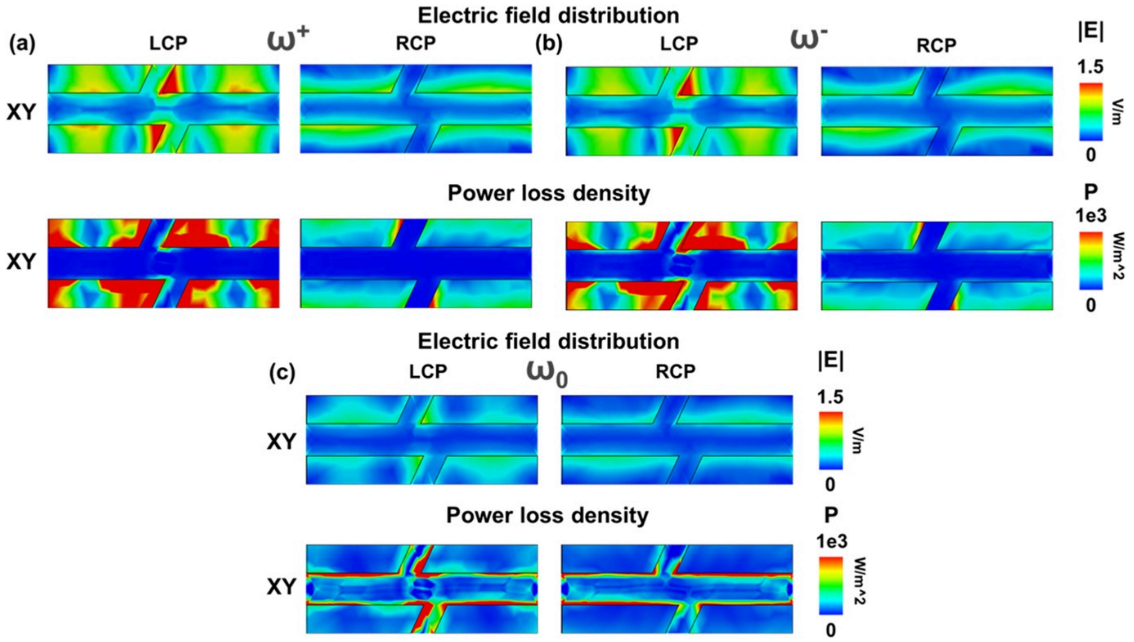

Figure 4. Simulated electric field distributions and power loss density distributions in *XY* plane at the Al-Al2O3 interface under LCP and RCP illumination at the frequencies of (a) ω^+, (b) ω^-, and (c) ω_0.

at the PMMA phonon vibrational frequency ω_0 is maintained throughout the GST-225 phase transition process. It is noted that EIT-like phenomena have also been reported in various metasurface platforms [43–46]. The CD spectrum mapping also shows the mode splitting feature and anti-crossing behavior of the coupled phonon–plasmon modes. When the plasmonic resonance matches the molecular phonon vibrational resonance, the CD value reaches 0.53 at the frequency ω^+ and 0.52 at the frequency ω^- but drops to 0.14 at the phonon vibrational frequency ω_0, exhibiting the high contrast in CD value variation around the phonon vibrational frequency. The simulation result in figure 5(b) shows a good agreement with the experimental result.

Furthermore, an analytical model is used to describe the interaction between the plasmonic resonance mode of the metasurface and the phonon vibrational mode of PMMA molecules under LCP and RCP excitation. The absorption spectrum of the metasurface-molecule coupled system can be calculated with the following equation [47]:

$$\boldsymbol{A} = 1 - \left| \frac{2\gamma_r}{\boldsymbol{j}(\omega - \omega_0) + (\gamma_r + \gamma_a) + \left(\frac{\mu^2}{j(\omega - \omega_m) + \gamma_m}\right)} - 1 \right|^2 \tag{1}$$

where $\boldsymbol{\omega_0}$ and $\boldsymbol{\omega_m}$ are the resonance frequencies of the metasurface mode and the molecule vibrational mode, respectively. γ_r and γ_a are the radiation and absorption losses of the metasurface mode, while γ_m is the absorption loss of molecule vibrational mode. $\boldsymbol{\mu}$ represents the coupling strength between

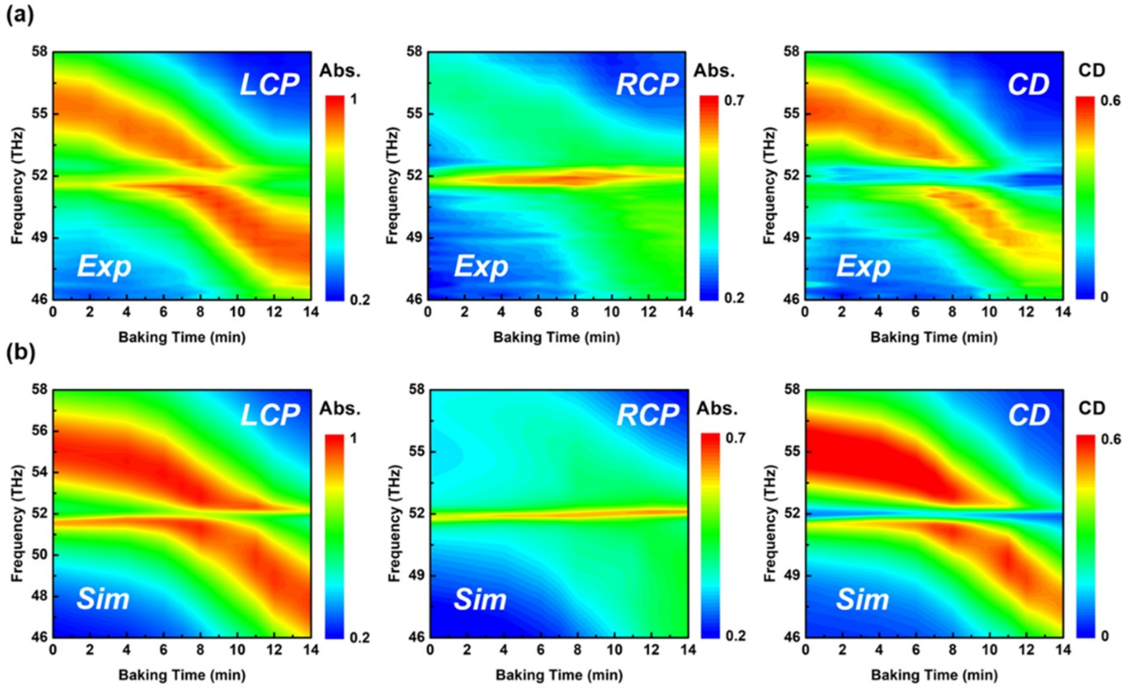

Figure 5. (a) Measured and (b) simulated contour plots of the absorption spectra under LCP and RCP illumination and the CD spectra as a function of baking time.

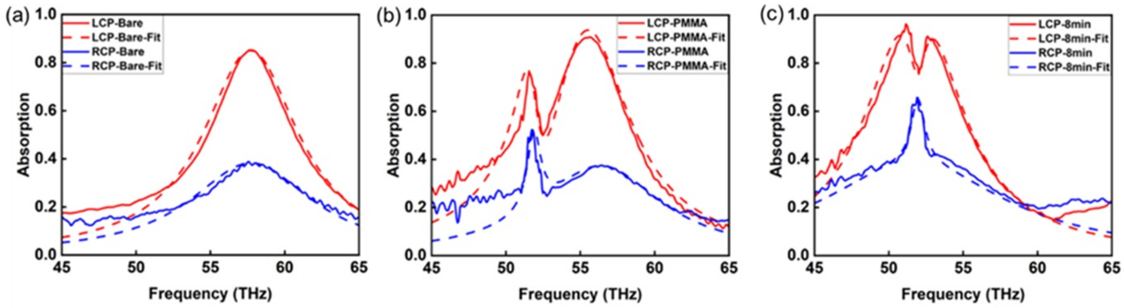

Figure 6. The fitted absorption spectra based on the analytical model (dashed lines) along with the measured absorption spectra (solid lines) for (a) bare metasurface before PMMA coating, metasurface after PMMA coating at the baking time of (b) 0 min and (c) 8 min, under LCP and RCP incidence.

the metasurface mode and the molecule vibrational mode. The fitted absorption spectra based on the analytical model are depicted as the dashed lines in figure 6 for bare metasurface before PMMA coating, metasurface after PMMA coating at the baking time of 0 min and 8 min. The analytically fitted curves show good agreement with the experimental data, and the fitting parameters used in the model are summarized in table 1. For PMMA molecules, $\omega_m = 1733\ \mathrm{cm}^{-1}$ and $\gamma_m = 16.5\ \mathrm{cm}^{-1}$ are used. It is observed that the undercoupling condition with $\gamma_r < \gamma_a$ is achieved between the metasurface-molecule coupled system and LCP incident light, whereas the overcoupling condition with $\gamma_r > \gamma_a$ is exhibited when the metasurface interacts with RCP incident light. It is noted that the μ values under LCP incidence are larger than those under RCP incidence, suggesting the stronger interactions between the metasurface plasmonic mode and the molecule phonon vibrational mode under LCP case. At the baking time of 0 min, ω_0 is off resonance with ω_m which results in a Fano-like spectral feature under LCP illumination. At the baking time of 8 min, ω_0 is tuned to overlap with ω_m, leading to the distinct mode splitting features under LCP incidence. It is worth noting that the tunable phonon–plasmon coupling achieved in the metasurface-molecule coupled system can be used for mid-infrared label-free molecular sensing. The demonstrated phase-change metasurface can be dynamically tuned on resonance with different molecular vibrational fingerprints, and the absorption spectral features of the coupled system under LCP and RCP incidence can be used for the detection of molecule amount and concentration.

Table 1. Fitting parameters in the analytical model of absorption spectra.

	ω_0 (cm^{-1})	γ_r (cm^{-1})	γ_a (cm^{-1})	μ (cm^{-1})
LCP-Bare	1925	40	90	0
RCP-Bare	1926	150	18	0
LCP-PMMA	1827	50	80	50
RCP-PMMA	1880	150	17	25
LCP-8 min	1726	50	80	33
RCP-8 min	1724	230	27	23

3. Conclusion

In summary, the coupling between the mid-infrared phonon vibrational mode of PMMA molecules and the tunable plasmonic resonance of phase-change chiral metasurfaces under circularly polarized light illumination is demonstrated. The plasmonic resonance of the designed chiral metasurface is thermally tuned across the phonon vibrational resonance of PMMA molecules by controlling the phase transition process in the GST-225 layer. The mode splitting features and anti-crossing behavior in the absorption spectra and the CD response of the metasurface coated with PMMA molecules under LCP and RCP incident light are investigated as a function of baking time. The electric field and power loss density distributions of the resonant modes under LCP and RCP illumination are further analyzed to understand the underlying mechanism of the circular polarization-dependent phonon–plasmon coupling. The demonstrated thermally tuned molecule-metasurface coupling will offer great potential for numerous applications including ultrasensitive chiral molecular sensing, enantiomer detection, biomedical diagnostics, polarization-encoded communication, and thermal emission control.

Data availability statement

All data that support the findings of this study are included within the article (and any supplementary files).

Acknowledgments

The authors acknowledge the support from the National Science Foundation ECCS-2230069, ECCS-2230071, and U.S. Department of Energy (DE-AC02-06CH11357). Work performed at the Center for Nanoscale Materials, a U.S. Department of Energy Office of Science User Facility, was supported by the U.S. DOE, Office of Basic Energy Sciences, under Contract No. DE-AC02-06CH11357. The authors acknowledge the support from the Intelligent Systems Center and the facility support from the Materials Research Center at Missouri S&T.

Conflict of interest

The authors have no conflicts of interest to disclose.

ORCID iDs

Haotian Tang 0000-0002-1855-4357
Xiaodong Yang 0000-0001-9031-3155
Jie Gao 0000-0003-0772-4530

References

[1] Yu N F and Capasso F 2014 Flat optics with designer metasurfaces *Nat. Mater.* **13** 139–50

[2] Kildishev A V, Boltasseva A and Shalaev V M 2013 Planar photonics with metasurfaces *Science* **339** 1232009

[3] Liu Y *et al* 2022 Negative refraction in twisted hyperbolic metasurfaces *Nanophotonics* **11** 1977–87

[4] Liu Y, Wang G P, Pendry J B and Zhang S 2022 All-angle reflectionless negative refraction with ideal photonic Weyl metamaterials *Light Sci. Appl.* **11** 276

[5] Zheng B, Ren H, An S, Tang H, Li H, Haerinia M, Dong Y, Fowler C and Zhang H 2021 Tunable metasurface with dynamic amplitude and phase control *IEEE Access* **9** 104522–9

[6] Intaravanne Y, Han J, Wang R, Ma A, Li S, Chen S and Chen X 2021 Phase manipulation-based polarization profile realization and hybrid holograms using geometric metasurface *Adv. Photonics Res.* **2** 2000046

[7] Liu W, Wang S R, Dai J Y, Zhang L, Chen Q, Cheng Q and Cui T J 2024 Arbitrarily rotating polarization direction and manipulating phases in linear and nonlinear ways using programmable metasurface *Light Sci. Appl.* **13** 172

[8] Hsiao H-H, Chen Y H, Lin R J, Wu P C, Wang S, Chen B H and Tsai D P 2018 Integrated resonant unit of metasurfaces for broadband efficiency and phase manipulation *Adv. Opt. Mater.* **6** 1800031

[9] Akselrod G M, Huang J, Hoang T B, Bowen P T, Su L, Smith D R and Mikkelsen M H 2015 Large-area metasurface perfect absorbers from visible to near-infrared *Adv. Mater.* **27** 8028–34

[10] Zeng X, Rosenmann D, Czaplewski D A, Gao J and Yang X 2022 Mid-infrared chiral metasurface absorbers with split-ellipse structures *Opt. Commun.* **525** 128854

[11] Ouyang L, Wang W, Rosenmann D, Czaplewski D, Gao J and Yang X 2018 Near-infrared chiral plasmonic metasurface absorbers *Opt. Express* **26** 31484–9

[12] Janneh M, Marcellis A D, Palange E, Tenggara A T and Byun D 2018 Design of a metasurface-based dual-band terahertz perfect absorber with very high Q-factors for sensing applications *Opt. Commun.* **416** 152–9

[13] Wu P C, Sokhoyan R, Shirmanesh G K, Cheng W-H and Atwater H A 2021 Near-infrared active metasurface for dynamic polarization conversion *Adv. Opt. Mater.* **9** 2100230

[14] Chatterjee J, Mohan A and Dixit V 2022 Ultrawideband RCS reduction of planar and conformal surfaces using ultrathin polarization conversion metasurface *IEEE Access* **10** 36563–75

[15] Deng Y, Wu C, Meng C, Bozhevolnyi S I and Ding F 2021 Functional metasurface quarter-wave plates for simultaneous polarization conversion and beam steering *ACS Nano* **15** 18532–40

[16] Zeng X, Rosenmann D, Czaplewski D A, Gao J and Yang X 2023 Chiral metasurfaces of wavy rectangle resonators with tunable circular dichroism *Optik* **286** 171024

[17] Fiuza-Maneiro N, Mendoza-Carreño J, Gómez-Graña S, Alonso M I, Polavarapu L and Mihi A 2024 Inducing efficient and multiwavelength circularly polarized emission from perovskite nanocrystals using chiral metasurfaces *Adv. Mater.* **36** 2413967

[18] Zhu Y, Song H, Liu R, Mu Y, Gedda M, Alodhay A N, Ying L and Gan Q 2025 On-site quantitative detection of fentanyl in heroin by machine learning-enabled SERS on super absorbing metasurfaces *npj Nanophoton.* **2** 7

[19] Cabre A, Verdaguer X and Riera A 2022 Recent advances in the enantioselective synthesis of chiral amines via transition metal-catalyzed asymmetric hydrogenation *Chem. Rev.* **122** 269–339

[20] John-Herpin A, Kavungal D, Mucke L V and Altug H 2021 Infrared metasurface augmented by deep learning for monitoring dynamics between all major classes of biomolecules *Adv. Mater.* **33** 2006054

[21] Iwanaga M, Hironaka T, Ikeda N, Sugasawa T and Takekoshi K 2023 Metasurface biosensors enabling single-molecule sensing of cell-free DNA *Nano Lett.* **23** 5755–61

[22] Michel A K U, Wuttig M and Taubner T 2017 Design parameters for phase-change materials for nanostructure resonance tuning *Adv. Opt. Mater.* **5** 1700261

[23] Morden D, Smith E M, Avrutsky I, Hendrickson J R, Agha I and Vangala S 2022 Tunable angle-independent mid-infrared optical filters using GST-based micro resonator arrays *Opt. Mater. Express* **12** 1043–54

[24] Liang Y, Lin H, Lin S, Wu J, Li W, Meng F, Yang Y, Huang X, Jia B and Kivshar Y 2021 Hybrid anisotropic plasmonic metasurfaces with multiple resonances of focused light beams *Nano Lett.* **21** 8917–23

[25] Syong W-R, Fu J-H, Kuo Y-H, Chu Y-C, Hakami M, Peng T-Y, Lynch J, Jariwala D, Tung V and Lu Y-J 2024 Enhanced photogating gain in scalable MoS_2 plasmonic photodetectors via resonant plasmonic metasurfaces *ACS Nano* **18** 5446–56

[26] Jones R R *et al* 2023 Dense arrays of nanohelices: Raman scattering from achiral molecules reveals the near-field enhancements at chiral metasurfaces *Adv. Mater.* **35** 2209282

[27] Min S *et al* 2021 Ultrasensitive molecular detection by imaging of centimeter-scale metasurfaces with a deterministic gradient geometry *Adv. Mater.* **33** 2100270

[28] Wang Q, Chen Y, Mao J, Yang F and Wang N 2023 Metasurface-assisted terahertz sensing *Sensors* **23** 5902

[29] Yesilkoy F, Arvelo E R, Jahani Y, Liu M, Tittl A, Cevher V, Kivshar Y and Altug H 2019 Ultrasensitive hyperspectral imaging and biodetection enabled by dielectric metasurfaces *Nat. Photon.* **13** 390–6

[30] Rippa M *et al* 2022 Plasmonic metasurfaces for specific SERS detection of Shiga toxins *ACS Appl. Mater. Interfaces* **14** 4969–79

[31] Hu J *et al* 2023 Rapid genetic screening with high quality factor metasurfaces *Nat. Commun.* **14** 4486

[32] Siegel J, Kim S, Fortman M, Wan C, Kats M A, Hon P W C, Sweatlock L, Jang M S and Brar V W 2024 Electrostatic steering of thermal emission with active metasurface control of delocalized modes *Nat. Commun.* **15** 3376

[33] Li J, Li Z, Liu X, Maslovski S and Shen S 2022 Active control of thermal emission by graphene-nanowire coupled plasmonic metasurfaces *Phys. Rev. B* **106** 115416

[34] Jing L, Liu X, Salihoglu H, Luo X, Yun H S, Wang Z and Shen S 2023 Electrically driven nanoantenna metasurface for coherent thermal emission *Appl. Phys. Lett.* **123** 161101

[35] Nolen J R, Overvig A C, Cotrufo M and Alù A 2024 Local control of polarization and geometric phase in thermal metasurfaces *Nat. Nanotechnol.* **19** 726–33

[36] Tittl A, Michel A K U, Schäferling M, Yin X, Gholipour B, Cui L, Wuttig M, Taubner T, Neubrech F and Giessen H 2015 A switchable mid-infrared plasmonic perfect absorber with multispectral thermal imaging capability *Adv. Mater.* **27** 4597–603

[37] Tang B, Li Z, Palacios E, Liu Z, Butun S and Aydin K 2017 Chiral-selective plasmonic metasurface absorbers operating at visible frequencies *IEEE Photonics Technol. Lett.* **29** 295–8

[38] Wan W, Yang X and Gao J 2016 Strong coupling between mid-infrared localized plasmons and phonons *Opt. Express* **24** 12367–74

[39] Rakić A D, Djurišić A B, Elazar J M and Majewski M L 1998 Optical properties of metallic films for vertical-cavity optoelectronic devices *Appl. Opt.* **37** 5271–83

[40] Kischkat J *et al* 2012 Mid-infrared optical properties of thin films of aluminum oxide, titanium dioxide, silicon dioxide, aluminum nitride, and silicon nitride *Appl. Opt.* **51** 6789–98

[41] Shportko K, Kremers S, Woda M, Lencer D, Robertson J and Wuttig M 2008 Resonant bonding in crystalline phase-change materials *Nat. Mater.* **7** 653–8

[42] Zhang X, Qiu J, Li X, Zhao J and Liu L 2020 Complex refractive indices measurements of polymers in visible and near-infrared bands *Appl. Opt.* **59** 2337–44

[43] Nourinovin S, Rahman M M, Naftaly M, Philpott P P, Abbasi Q H and Alomainy A 2024 Highly sensitive terahertz metasurface based on electromagnetically induced transparency-like resonance in detection of skin cancer cells *IEEE Trans. Biomed. Eng.* **71** 2180–8

[44] Teymoori M and Yalcinkaya A D 2024 Fano resonances induced by strong conductive coupling in cross-shaped metasurfaces for tunable EIT-like phenomena *Sci. Rep.* **14** 18556

[45] Zhao X, Huang R, Du X, Zhang Z and Li G 2024 Ultrahigh-Q metasurface transparency band induced by collective–collective coupling *Nano Lett.* **24** 1238–45

[46] Ren K, Wang S, Ren X, Peng W, Zhang H and Jia D 2024 Multi-band tunable electromagnetically induced transparencies based on active metasurface with polarization-independent property *J. Appl. Phys.* **57** 255102

[47] Li D, Zhou H, Ren Z, Xu C and Lee C 2025 Tailoring light–matter interactions in overcoupled resonator for biomolecule recognition and detection *Nano-Micro Lett.* **17** 10